BLEscope: A Bluetooth Low Energy (BLE) Microscope for Wireless Multicontrast Functional Imaging

Subhrajit Das, Janaka Senarathna, Yunke Ren, Vu Dinh, Mingyao Ying, Ralph Etienne-Cummings, *Fellow, IEEE* and Arvind P. Pathak

***Abstract* – Recent advances in low-power wireless-capable system-on-chips (SoCs) have accelerated diverse Internet of Things (IoT) applications, encompassing wearables, asset monitoring, and more. Concurrently, the field of neuroimaging has experienced escalating demand for lightweight, untethered, low-power systems capable of imaging in small animals. This article explores the feasibility of using a low-power asset monitoring system as the basis of a new architecture for fluorescence and hemodynamic contrast-based wireless functional imaging. The core system architecture hinges on the fusion of a Bluetooth Low Energy (BLE) 5.2 SoC and a low-power 560×560, 8-bit monochrome CMOS image sensor module. Successful integration of a multicontrast optical front-end consisting of a fluorescence channel (FL) and an intrinsic optical signal (IOS) channel resulted in the creation of a wireless microscope called 'BLEscope'. Next, we developed a wireless (i.e. BLE) protocol to remotely operate the BLEscope via a laptop and acquire in vivo images at 1 frame per second (fps). We then conducted a comprehensive characterization of the BLEscope to assess its optical capabilities and power consumption. We report a new benchmark for continuous wireless imaging of ~1.5 hours with a 100 mAh battery. Via the FL channel of the BLEscope, we successfully tracked the kinetics of an intravenously injected fluorescent tracer and acquired images of fluorescent brain tumor cells in vivo. Via the IOS channel, we characterized the differential response of normal and tumor-associated blood vessels to a carbogen gas inhalation challenge. When miniaturized, the BLEscope will result in a new class of low-power, implantable or wireless microscopes that could transform preclinical and clinical neuroimaging applications.**

***Index Terms*—Bluetooth Low Energy (BLE), microscopy, multicontrast, neuroimaging, smartphone, low-power, wireless.**

This work was supported by NIH/NCI grant nos. 2R01CA196701-06A1 and 5R01CA237597-04.

Subhrajit Das is a Ph.D. student in the Dept. of Electrical and Computer Engineering at Johns Hopkins University, Baltimore, MD 21218 USA (sdas32@jhu.edu).

Dr. Janaka Senarathna is an Instructor in the Russell H. Morgan Dept. of Radiology and Radiological Science at the Johns Hopkins University School of Medicine, Baltimore, MD 21205 USA (dsenara1@jhu.edu).

Yunke Ren is a PhD student in the Dept. of Biomedical Engineering at the Johns Hopkins University School of Medicine, Baltimore, MD 21205 USA (yren26@jh.edu).

Vu Dinh is a Research Technologist in the Russell H. Morgan Dept. of Radiology and Radiological Science at the Johns Hopkins University School of Medicine, Baltimore, MD 21205 USA (vdinh2@jh.edu).

Dr. Mingyao Ying is an Associate Professor in the Dept. of Neurology at the Johns Hopkins University School of Medicine and the Kennedy Krieger Institute, Baltimore, MD 21205 USA (mying1@jh.edu).

Dr. Ralph Etienne-Cummins is a Professor in the Dept. of Electrical and Computer Engineering at Johns Hopkins University, Baltimore, MD 21218, USA (retienn1@jh.edu).

I. Introduction

To elucidate the correlation between neurovascular changes and behavior in unanesthetized or freely moving animals, several teams have developed innovative miniaturized microscopes or miniscopes [1]. These include the UCLA miniscope [2], FinchScope [3], and miniScope [4], all of which have "open-source" (i.e. publicly available) circuit and optical designs and the capability to record behaviorally relevant neural signals when mounted on the heads of rodents. However, a crucial limitation of many extant miniscope systems [1-3, 5] is their reliance on tethers or wires for data acquisition and control. These tethers can hinder the natural behavior of animals during neuroscientific experiments and pose challenges when simultaneously imaging multiple animals, as they can become entangled. Therefore, there is a pressing need for miniscopes that can operate without a tether. However, tetherless operation requires an onboard battery to power the miniscope, which creates a significant obstacle because the weight of even a small battery (e.g. 40 mAh LiPo) can be a significant fraction of the body weight of a rodent (e.g. a 5 g battery compared to a mouse weighing 25 g), thereby affecting its natural behavior. To address this, a wireless miniscope for neuronal imaging was developed using an off-the-shelf NTSC (National Television Standards Committee) analog transmitter [3]. This miniscope could image for up to 30 min on a 50 mAh battery weighing 1 g. A drawback of this approach was that analog NTSC video transmission [6], once a stalwart of video broadcasting, exhibits limitations for video or image transmission relative to contemporary alternatives like BLE (Bluetooth Low Energy), Wi-Fi, and ZigBee. Primarily, NTSC suffers from limited spatial resolution and image quality due to the need for the substantial data reduction required to transmit analog video signals over the available bandwidth. Specifically, a key NTSC data reduction technique is interlacing, wherein each video frame is divided into two fields, reducing the number of scan lines displayed at any given moment and effectively halving the data rate. Additionally, color encoding in NTSC uses the YUV scheme, where the color information is subsampled to save bandwidth. Moreover, NTSC is susceptible

Dr. Arvind P. Pathak is a Professor in the Russell H. Morgan Dept. of Radiology and Radiological Science and Dept. of Biomedical Engineering at the Johns Hopkins University School of Medicine, as well as the Dept. of Electrical and Computer Engineering at Johns Hopkins University and the Sidney Kimmel Comprehensive Cancer Center, Baltimore, MD 21205, USA (apathak2@jhmi.edu).

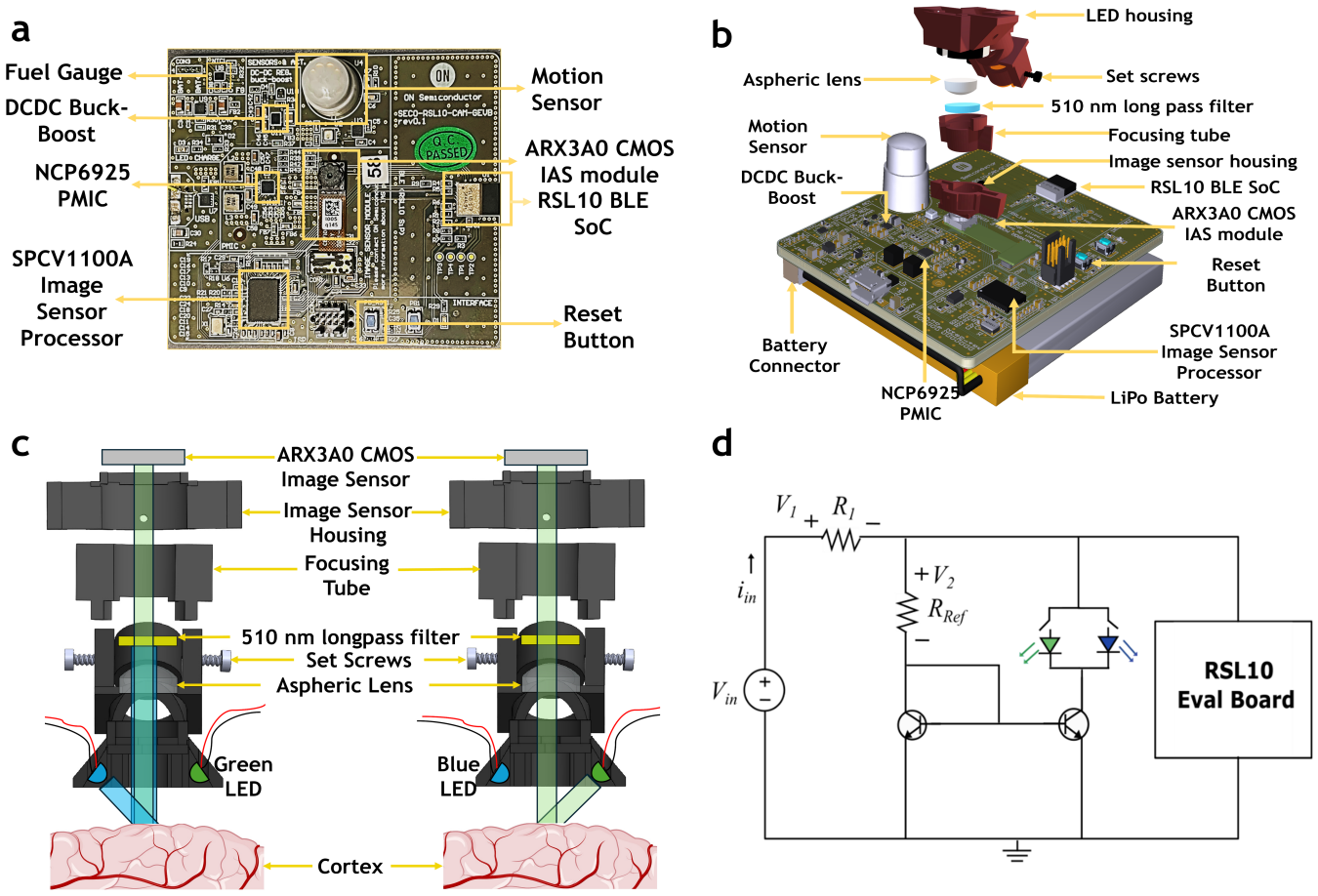

Fig. 1. A BLE 5.2 capable multicontrast microscope for functional imaging. (a) Evaluation board utilized in the BLEscope features: the low-power CMOS ARX3A0 image sensor; the RSL10 Bluetooth Low Energy (BLE) System on Chip (SoC); SPCV1100A image sensor processor (ISP); NCP6925 Power Management Integrated Circuit (PMIC); DCDC Buck-Boost converter; motion sensor; and fuel gauge. (b) Exploded view of the 'BLEscope' revealing its components, including the dual LED housing, aspheric lens, and focusing tube. Also shown is the LiPo battery (1700 mAh, 3.7 V) with the evaluation board as depicted in (a). The arrangements of the key components of the evaluation board like RSL10 BLE Soc, the CMOS ARX3A0 image sensor, the SPCV1100A Image Sensor Processor (ISP), and NCP6925 PMIC, with respect to the microscope are illustrated here. (c) Cross-sectional view of the BLEscope illustrating the optical and imaging paths for multicontrast imaging (i.e. FL and IOS). The optical system incorporates an aspheric lens and a 510 nm long-pass filter. All optical elements and the image sensor were located within the sensor housing and focusing tube. The blue and green LEDs were situated in the LED housing. During FL imaging, the blue LED (452±10 nm) acts as the excitation source for green fluorescent protein (GFP) or FITC, resulting in light emission at 530±20 nm. A 510 nm long-pass filter eliminates reflected light <510 nm, permitting only the 530±20 nm emission light. For IOS imaging, the green LED (530±20 nm) serves as the excitation source, with the image sensor detecting the scattered and reflected 530±20 nm light from the cortex. (d) Circuit schematic for powering the LEDs and the RSL10 smart-shot camera evaluation board**.** This circuit provided a constant current to the LEDs via the 1700 mAh, 3.7 V LiPo battery (V_{in}). The battery also powered the RSL10 smart shot camera evaluation board. V_1 is the voltage drop across R_1, while V_2 denotes the voltage drop across R_{Ref}.

to signal degradation, resulting in less reliable transmissions. This is because, in NTSC, video and audio signals are carried as continuous electromagnetic waves, making them vulnerable to external electromagnetic interference. Noise, such as radio frequency interference (RFI) and electromagnetic interference (EMI), can disrupt the analog signal, leading to visual artifacts like snow and ghosting on the screen, as well as audio disturbances. In contrast, BLE, Wi-Fi, and ZigBee offer the convenience of wireless connectivity and compatibility across a broad spectrum of devices, while NTSC hinges on a dedicated analog infrastructure, rendering it less versatile and adaptable within the evolving landscape of technology ecosystems. Furthermore, these newer transmission technologies provide robust encryption and security features, a facet in which NTSC is deficient, thereby ensuring the safeguarding of sensitive video or image data.

Consequently, there is a crucial need for a new class of devices that are lightweight (i.e. <4 g), exhibit ultra-low power consumption (i.e. <50 mW), and are capable of wireless data transmission for continuous, real-time functional imaging (i.e. 5-10 µm spatial resolution) in rodents without impeding their natural behavior. Low-power wireless transmission utilizing LoRa [7-9] that uses a spread-spectrum modulation technique to transmit data over a long-range, may be feasible for real-time video streaming. However, its relatively low data transmission rate (18-37 kbps) with respect to Wi-Fi and BLE (1-2 Mbps) renders it unsuitable for many bioimaging applications. Additionally, LoRa is a relatively nascent technology concerning market maturity, thereby affecting the widespread availability of compatible devices and support. Furthermore, it is worth noting that most open-source wireless miniscopes [3, 4] have current requirements ranging from 100-300 mA, which constrains their continuous imaging ability when running on a battery.

To address these power and wireless transmission limitations inherent in developing a wireless microscope, we explored the feasibility of leveraging a low-power asset monitoring and security surveillance system as the foundational architecture. After a thorough evaluation and comparison of available BLE image transfer options (see **Suppl. Table 1**), we selected the RSL10 smart shot camera evaluation board (On-Semiconductor Corp., Scottsdale, AZ) [10]. This choice was driven by the board's incorporation of a Bluetooth Low Energy 5.2 (BLE5.2) System-on-Chip (SoC) RSL10 [11], which utilizes an ARM Cortex-M3 microcontroller, along with a low-power CMOS image sensor, ARX3A0 [12] (both from On-Semiconductor Corp., Scottsdale, AZ). Our selection was influenced by several key factors. The RSL10 board offers manufacturer-provided firmware that optimizes wireless image transmission, while providing higher resolution and a larger field-of-view (FOV) than other boards and maintains the low power consumption essential for prolonged imaging (see **Suppl. Table 1**). The central position of the ARX3A0 image sensor on the board further simplified its integration with a microscope via the addition of an optical front end [1]. This integration enabled us to demonstrate the feasibility of continuous functional imaging in mice. Our wireless microscope (BLEscope) successfully streamed images from a ~2 mm² FOV in the murine sensorimotor cortex at 1 frame per second (fps) over BLE to a smartphone or laptop, enabling seamless wireless imaging and remote operation.

In this paper, we present the implementation and validation of this wireless 'BLEscope'. BLEscope is capable of streaming 560×560, 8-bit monochrome videos at 1 frame per second (fps) to any Bluetooth-enabled device. Additionally, the microscope base included two light emitting diodes (LEDs) for multicontrast imaging (i.e. fluorescence or FL and intrinsic optical signal or IOS) that were controlled by a constant current source. Multicontrast imaging is not a feature currently available in the UCLA miniscope [2], FinchScope [3], or miniScope [4]. Furthermore, the BLEscope is estimated to be capable of acquiring images down to a depth of ~500 µm in the cortex [13]. We extensively characterized the BLEscope, including its optical performance via optical targets, and current consumption under two different image acquisition modes (i.e. *single image capture* and *streaming*). Via in vivo experiments in anesthetized animals (due to the size of this proof-of-concept system), we demonstrated BLEscope's versatility for functional imaging applications. To the best of our knowledge, this is the first report of a fully wireless microscope capable of transmitting real-time multicontrast images over BLE to any smartphone, laptop, or PC. This novel approach sets the stage for a fully tetherless microscope with a completely miniaturized architecture in the future.

II. Materials and Methods

A. Microscope Design and Functionality

The BLEscope described in this paper utilized an RSL10 smart shot camera evaluation board (**Fig. 1a**) combined with a 3D-printed microscope (**Fig. 1b**) [1]. The microscope was mounted on top of the image sensor module as shown in **Fig. 1b.** The microscope employed a long-pass filter with a cutoff of 510 nm to prevent the transmission of blue excitation light, while permitting light from the green LED and FL emission as shown in **Fig. 1c**. The microscope also incorporated an aspheric lens (f = 4.6 mm) to focus the image onto the CMOS image sensor (ARX3A0). We did not employ a VCSEL, or synchronization LEDs as were used in [1] because BLEscope's design did not include laser speckle contrast imaging. BLEscope has an excitation module that incorporated two LEDs for illumination, driven by a constant current source implemented as a current mirror circuit, as shown in **Fig. 1d**. LEDs were manually switched for multicontrast functional imaging. In **Fig. 1d**, R_{Ref} was set to 10 k**Ω** to drive the green LED (530±20 nm) illumination for intrinsic optical signal (IOS) imaging [14], which is an imaging technique that utilizes the light absorption by total hemoglobin (HbT) to visualize cerebral blood volume (CBV) in the brain. R_{Ref} was set to 3.2 k**Ω** or 2.2 k**Ω** to drive blue LED (452 ± 10 nm) illumination used for fluorescence (FL) imaging [15]. R_1 was a shunting resistor that was used to measure the current consumed by the BLEscope. It was set to 0.1**Ω** with a tolerance of 1% to minimize the voltage drop across the resistor. The entire system was powered by a 3.7 V LiPo battery (i.e. V_{in} in **Fig. 1d**). To ensure versatility, the BLEscope could be controlled via a smartphone application, laptop, or PC in two image acquisition modes: (i) a "single image capture" mode, and (ii) a *streaming* mode for continuous video-like acquisition. To lower power consumption during image acquisition, the CMOS image sensor was operated at 1 fps, although it could be operated at 360 fps. Specifically, with the limited data transmission rate of BLE5.2, we could achieve a maximum wireless image transfer rate of 1 fps for the BLEscope. This was also the minimum frame rate necessary to demonstrate the utility of this BLE architecture for wireless functional imaging.

B. Wireless System Architecture Overview

The system architecture of the smart shot camera evaluation board is illustrated in **Fig. 2**. It comprised of a low-power system-on-chip (SoC) RSL10 for wireless data transceiving; a FAN49100 buck/boost converter [16] for supplying a constant voltage; an NCP6925 power management [17] integrated circuit (PMIC); and an Image Access System (IAS) module housing the ARX3A0 low-power CMOS image sensor (all ICs were provided by On-Semiconductor Corp., Scottsdale, AZ) [12]. The power supply of the RSL10 smart shot camera was designed by the manufacturer for low-power operation via the multi-rail power delivery feature of the NCP6925 PMIC. This multi-rail Power Management Integrated Circuit (PMIC) is comprised of two DC-DC converters and five Linear Dropout Regulators (LDOs). The two DC-DC converters were used to supply 3.3 V and 1.3 V to the SPCV1100A image sensor processor (ISP), while three of the five LDOs provided power at 1.2 V, 2.7 V, and 1.8 V, respectively to the image sensor(as shown in **Fig. 2**). By

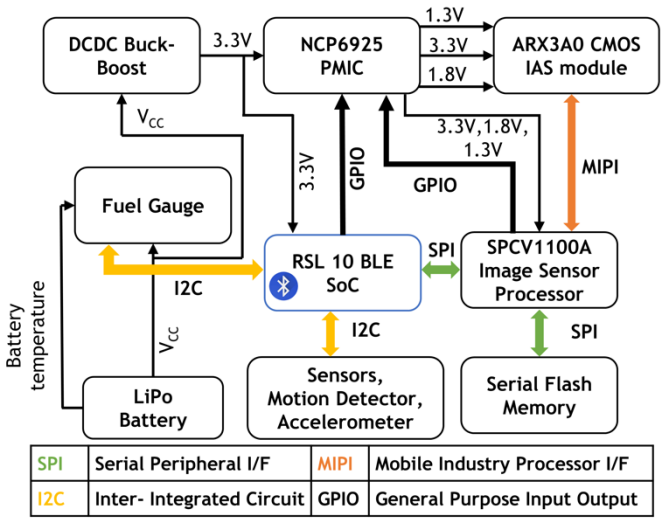

Fig. 2. BLEscope architecture and wireless control. The system architecture of the RSL10 evaluation board comprised of: RSL10 BLE SoC; ARX3A0 image sensor module; SPCV1100A ISP; environmental sensors (e.g. accelerometer and motion detector); a DCDC buck-boost converter; NCP6925 PMIC; and a fuel gauge. A LiPo battery powered this architecture. The RSL10 BLE SoC communicates with the SPCV1100A ISP over a Serial Peripheral Interface (SPI) shown in green. SPCV1100A ISP receives image data from the ARX3A0 image sensor over the Mobile Industry Processor Interface (MIPI). The NCP6925 PMIC communicates over GPIO with the RSL10 BLE SoC to manage the powering up sequence of the ARX3A0 image sensor and the SPCV1100A ISP. A serial flash memory holds the instructions for control of the ARX3A0 image sensor by SPCV1100A ISP.

consolidating these functions in a single chip, the manufacturer reduced component count and space requirements, and eliminated the need for individual regulator packages. Additionally, the PMIC orchestrated the power-up and power-down sequences for the SPCV1100A ISP and ARX3A0 CMOS image sensor, ensuring they received power in the correct order. Moreover, this PMIC incorporated support for low-power and deep sleep modes, enabling both the ISP and image sensor to enter energy-conserving states during periods of inactivity. This efficient management of power consumption contributed to prolonged battery life. The low-power PMIC (i.e. NCP6925), with the above-mentioned features, made the system particularly well-suited for long-term functional imaging applications. To achieve low-power image capture and processing, the evaluation board incorporated the SPCV1100A Image Sensor Processor (ISP, Sunplus IT, Taiwan) and the ARX3A0 CMOS image sensor. The ARX3A0 CMOS image sensor has a compact 1/10th inch optical format and consumes a mere 3.2 mW at 1 fps. Even when operating at 360 fps and a full resolution of 560×560 pixels, it only uses 122.7 mW [12], which is at least 100 mW lower than other miniscope image sensors, as summarized in **Table I**. The ARX3A0 also achieves a quantum efficiency of >90% from 450-550 nm. **Table I** compares the specifications of the ARX3A0 image sensor to sensors used by other open-source miniscopes, demonstrating that this off-the-shelf CMOS image sensor met our design criteria for a low-power, wireless microscope. The SPCV1100A ISP acts as a low-power camera controller responsible for managing and receiving image data from the

TABLE I
COMPARISON OF IMAGE SENSORS USED BY OPEN-SOURCE MINISCOPES (OPTIMAL SPECIFICATION IN EACH ROW IS IN **BOLD**)

Image sensor Microscope name	ARX3A0 (Current Study)	PYTHON480 UCLA miniscope [2]	MT9V022 miniScope [4]	OV7960 FinchScope [3]
Power at full resolution (mW)	**122.7**	226	320	225
Quantum efficiency (Range nm)	**90% (450-550 nm)**	56% (500-700 nm)	50% (550-650 nm)	Not available
Dynamic Range (dB)	**74.3 dB**	>59 dB	>55dB	Not available
Form Factor	**1/10''**	1/3.7''	1/3''	1/3.6''
Max image transfer rate (fps)	**360**	120	60	60
Pixel size (µm)	**2.2×2.2**	4.8×4.8	6.0×6.0	6.0×6.0
Resolution (pixels)	560×560	**808×608**	752×480	750×480

IAS module via a high-speed MIPI (Mobile Industry Processor Interface) interface. It also performed JPEG compression on the acquired images at a compression level of 40%. The SPCV1100A ISP relies on the NCP6925, an ultra-low power PMIC, to provide the supply voltage rails. The PMIC also provides power to the other voltage rails utilized by the ARX3A0 CMOS image sensor, to ensure low power consumption. JPEG-processed images were transferred to the RSL10 from the SPCV1100A ISP via a high-speed SPI (Serial Peripheral Interface). To provide a stable 3.3 V supply to the RSL10 and the power management unit (NCP6925), a low-power buck/boost converter (DC/DC) called FAN4910 [16], was employed. Note that the evaluation board's recharge feature was not utilized for any of the experiments.

C. Wireless Image Acquisition over BLE

Fig. 3 illustrates the operational flowchart for the BLEscope. The BLEscope is powered by a 3.7 V LiPo battery. The RSL10 initiates communication by advertising packets, and a MATLAB® script establishes a connection with the BLEscope. Four opcodes were used to control the BLEscope, as shown in the flowchart. Opcode 0x01 activated the "single capture" mode, which wakes up the ARX3A0 image sensor and the SPCV1100A ISP, enabling the image sensor to acquire an image. Subsequently, opcode 0x04 is sent to the BLEscope, prompting it to transmit image data back in chunks. A similar procedure occurs when opcode 0x02 is received; however, in this case, the ARX3A0 image sensor and the SPCV1100A ISP remain continuously active, and the MATLAB® script requests image data every second, resulting in continuous image streaming over BLE. Opcode 0x03 terminates all image acquisition and transfer activities. A detailed description of the wireless image acquisition process is provided in the

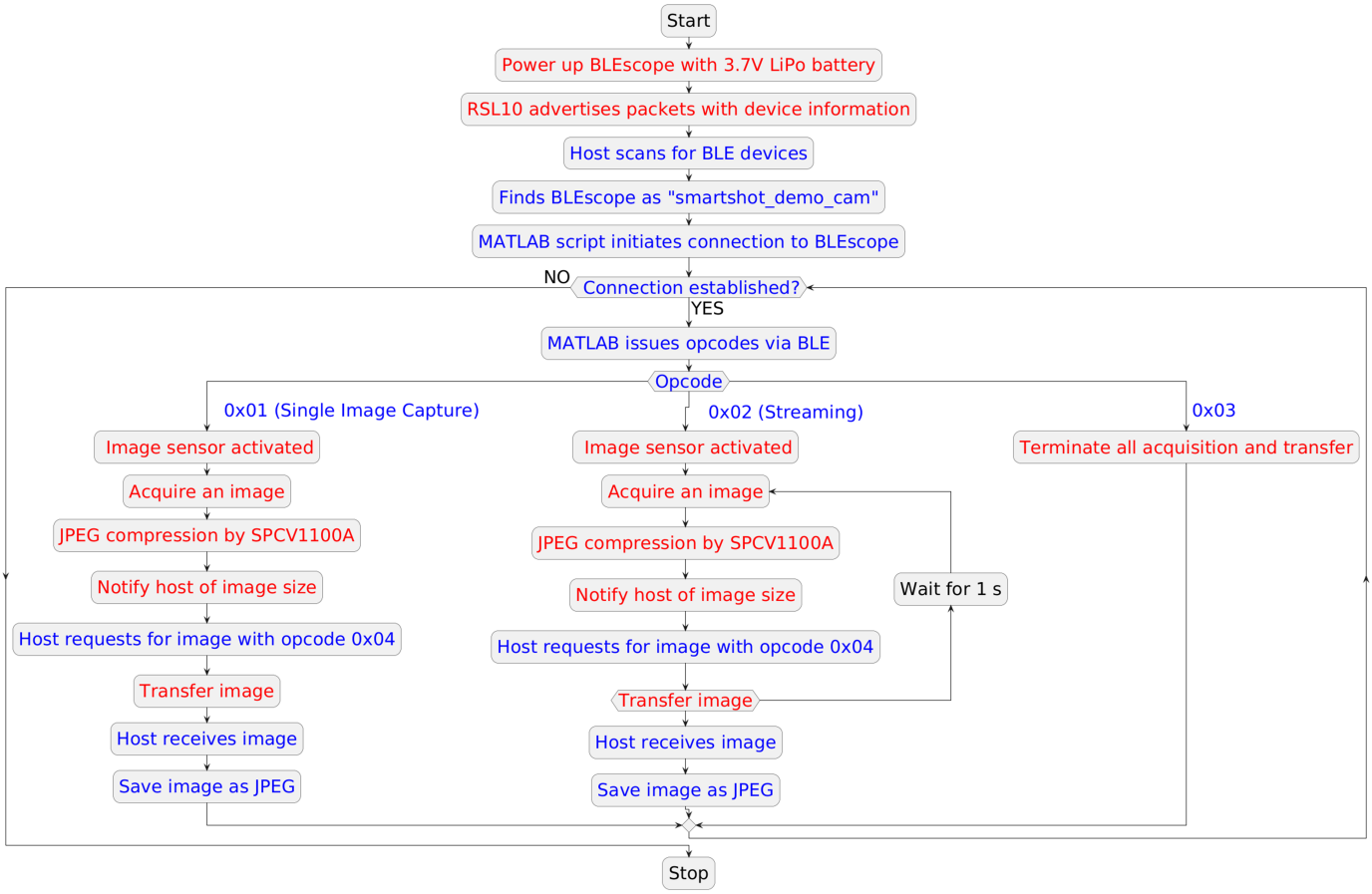

Fig. 3. Flowchart for wireless image acquisition over BLE. Upon powering up, the BLEscope begins advertising packets. A connection is then established via MATLAB®, which sends opcodes over BLE to control the BLEscope. Opcode 0x01 triggers single image capture mode, while 0x02 starts streaming mode. Next, the image sensor activates and initiates image acquisition. Acquired images are compressed to JPEG format by the SPCV1100A. When the host (can be a laptop, PC, or phone) requests for image data with opcode 0x04, the data is transferred in chunks to the host. The host then receives and saves the image data in JPEG format. The red font indicates the operations occurring on the RSL10 smartshot camera eval board, while the blue font indicates operations occurring on the host.

Supplementary Material. These opcodes were provided by On-Semiconductor as a part of the "Transfer" services used by their cell phone application for controlling the RSL10 evaluation board. For example, on starting the application, the phone scans for nearby BLE devices (**Fig. 4a**), following which the BLEscope shows up in the list as "smartshot_demo_cam" (**Fig. 4b**). On selecting that device, the BLEscope begins streaming images to the cell phone, which we can change to "single image capture" mode in the settings as shown in **Fig. 4d**. The phone application does not save data in the *streaming* mode but does save individual images to the cell phone's local memory via the "save" button as shown in **Fig. 4g**. For our experiments, we only used the live *streaming* mode shown in **Fig. 4c**.

D. *Experimental Setup for Imaging*

To characterize the BLEscope and test its performance, we required a stable setup and external focusing mechanism. This was achieved by designing a 3D-printed, L-shaped platform to position as shown in **Suppl. Fig. 1**. This platform was then mounted via screws on the arm of a stereotaxic frame as shown in **Figs. 5a, b**. The x-, y-, and z-axes micrometers of the stereotaxic frame provided three degrees of freedom for adjusting the BLEscope's position and focus. Another stabilized platform was used to hold the optical target or animal within the stereotaxic frame during imaging. The MATLAB® script saved images received over BLE in the local memory but did not provide an interactive live *streaming* mode to focus the BLEscope. Therefore, we used the *streaming* mode at 1 fps on the cell phone application provided by On-Semiconductor Corp. (**Fig. 4**) for focusing and finding the desired FOV. Once the FOV was identified, we disconnected the BLEscope from the cell phone application and connected it to the laptop to send control opcodes and receive images over BLE5.2.

E. *Characterization of the optical performance of the BLEscope*

To comprehensively characterize the magnification, spatial resolution, and FOV of the BLEscope, we imaged a positive 3×3" 1951 USAF optical target. The optical target was secured to the platform to minimize motion during image acquisition. The BLEscope was focused on the optical target to optimize image clarity and detail. Upon acquisition in the IOS channel, the image of the optical target underwent contrast inversion to facilitate the assessment of cross-sectional profiles of vertical and horizontal line pairs within three distinct elements of the target: group 6 element 5, group 6 element 6, and group 7

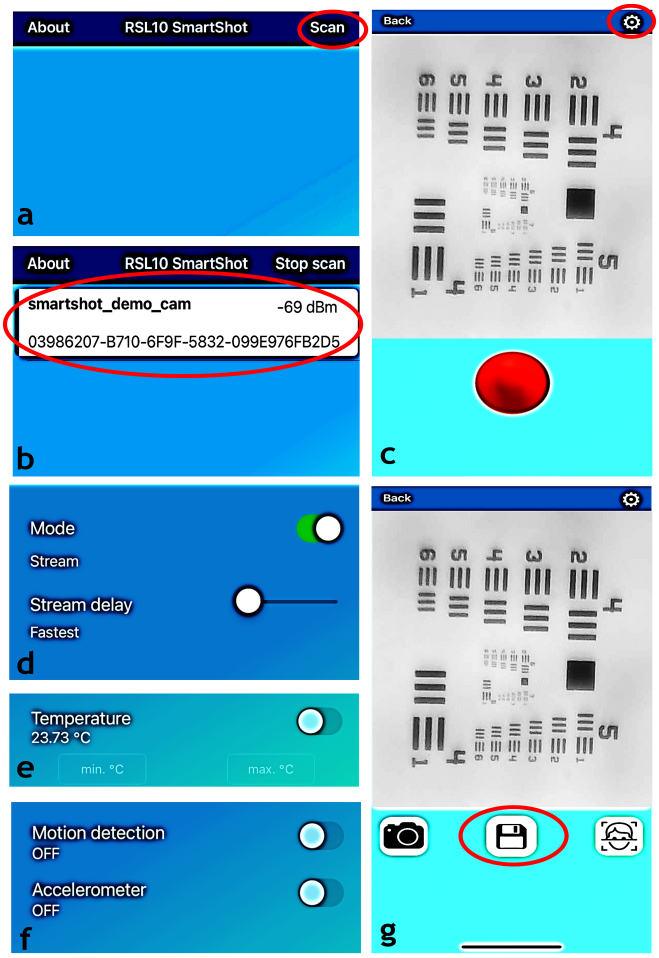

Fig. 4. Image capture and live streaming of a 1951 USAF optical target with the BLEscope via the phone application. (a). Upon starting the phone application, the user presses the *Scan* button to search for nearby Bluetooth-enabled devices. (b) The application detects the RSL10 smart shot camera evaluation board via transmitted information (packets) of its availability. Next, the user presses the *smartshot_demo_cam* button to connect to the BLEscope. (c) Live-streamed image from the BLEscope as viewed within the phone application. Users can start or stop the application by pressing the red button. Users can press the settings button to change the image acquisition mode. (d) On the "Settings" screen, the user can select the frame rate for streaming and toggle between "single image capture" and "streaming" modes. (e) The user can also set a temperature range, and if the temperature exceeds this limit, the BLEscope will automatically capture an image. (f) The user can also configure the motion detector and accelerometer settings to activate the microscope and capture images only when motion is detected. (g) The user can capture an image from the BLEscope by pressing the camera icon and saving it into the smartphone's local memory by pressing the save icon. Key presses are highlighted by red ellipses in each sub-panel.

element 1 (**Fig. 6a**). Each of these elements comprised of three horizontal and vertical line pairs, forming a standard reference for evaluating the resolution of the imaging system. To determine the finest resolvable line pairs, horizontal and vertical reference lines were drawn across the identified line pairs using the ImageJ software [18, 19]. Subsequently, their corresponding cross-sectional profiles were examined. The spatial derivatives of these lines were computed to identify local minima, indicative of the resolving capabilities of the imaging system. Further analysis involved plotting the number of peaks detected in the spatial derivative of intensity by varying the detection threshold from 0 to 50. This facilitated the

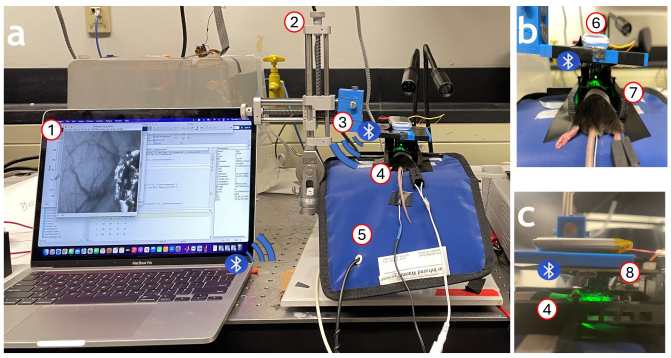

Fig. 5. Experimental setup for in vivo multicontrast functional imaging with the BLEscope. (a) Experimental setup showing an anesthetized mouse on the customized imaging platform. An Apple MacBook Air M1 (1) was used to communicate with the BLEscope and save images received over BLE. A stereotaxic frame (2) held the 3D-printed L-shaped platform (3) that supported the BLEscope in a stable position above the anesthetized animal (4), while streaming images to the laptop (1). (5) is the heating pad for maintaining the mouse's body temperature at 37° C. (b) Close up view of the L-shaped platform and anesthetized mouse**.** A LiPo battery (6) on top of the L-shaped platform (3) powers the BLEscope. A customized holder (7) was used to stabilize the mouse's head during imaging. (c) A lateral view of the setup showing the IOS channel of the BLEscope acquiring images under green light illumination through the cranial window of the anesthetized mouse (4).

identification of the finest resolvable line pairs per unit distance (lp/mm) within the optical target. From these analyses, the spatial resolution of the BLEscope was calculated using:

$$Resolution(\mu m) = \frac{1000}{\frac{lp}{mm}} \quad (1)$$

Magnification was calculated by dividing the length of the imaged line in one of the line pair groups by its actual length in the optical target. For calculating the FOV, the product of pixel size and spatial resolution was divided by magnification.

The BLEscope's fluorescence (FL) channel is designed to detect fluorescence emissions within the ~510-540 nm range. This range coincides with the illumination wavelengths (i.e. 530 ± 20 nm) employed for the intrinsic optical signal (IOS) channel. Consequently, the spatial resolution characterization performed with the IOS channel is considered to be similarly applicable to the FL channel of the BLEscope.

F. Animal Preparation for In Vivo Functional Imaging Experiments

All animal experiments were conducted in accordance with an approved Johns Hopkins University Animal Care and Use Committee (JHU ACUC) protocol (#MO22M159). The Johns Hopkins University animal facility is accredited by the American Association for the Accreditation of Laboratory Animal Care and meets the National Institutes of Health (NIH) standards as set forth in the "Guide for the Care and Use of Laboratory Animals". To assess the utility of the BLEscope for functional imaging, we conducted two in vivo experiments: the first tracked the transit of an intravascular fluorescent tracer within the cerebrovasculature, and the second assessed the vasodilatory response of the cerebrovasculature to carbogen gas (95% O_2 and 5% CO_2) inhalation in two brain tumor-bearing

mice. In addition, we measured the current of the BLEscope when imaging with IOS and fluorescence channels.

For in vivo experiments, we created a 3 mm diameter cranial window in four C57/BL6 mice as described in [20]. The mice were anesthetized using an intraperitoneal injection of a 0.15 ml volume comprising of a mixture of 80 mg/kg of ketamine and 8 mg/kg of xylazine. We also administered subcutaneous injections of 0.5 mL of dexamethasone (2 mg/ml) and buprenorphine (1 mg/ml) to manage any inflammation and pain. All surgical instruments were sterilized prior to use. The top of the skull was shaved and sterilized with betadine, and the animals' eyes were protected using an ophthalmic lubrication ointment. Each mouse was then placed in a stereotaxic frame, and its level of sedation assessed with a paw-pinch test. After confirming that an adequate depth of sedation had been achieved, we removed the skin above the calvarium with surgical scissors, and gently cleared away any remaining connective tissue with a scalpel. The center of the window was marked at 3 mm above the lambdoid suture and 3 mm to the right of the sagittal suture, and a 3 mm diameter cranial window was created with a dental drill (Wave Dental Carbide Handpiece Burs, Round, HP1/4). During drilling, cold saline was used to flush bone residue and cool the site. Once the cranial window was created, a 5 mm diameter glass coverslip was placed on it and secured with cyanoacrylate glue. Finally, dental cement was applied to cover any exposed areas.

The first animal experiment was designed to gauge current consumption, while the second was designed to track the in vivo kinetics of a fluorescent tracer. Next, we inoculated the brains of two additional mice with different concentrations of GL261-GFP brain tumor cells. These cells were maintained until the cultivation reached ~90% confluence in a T-flask, and their GFP expression was validated on a standard epifluorescence microscope. Next, cells were harvested and split into two 0.5 mL microcentrifuge tubes. The first tube contained 50,000 cells/µl, and the second 100,000 cells/µl. Subsequently, mice were anesthetized, and cranial windows were created as described above. Utilizing a Hamilton microsyringe, ~1 µL of the first tumor cell suspension (~50,000 cells) was injected at two depths within the brain of the third mouse. This process was repeated for the fourth mouse, ~1 µL of the second tumor cell suspension (~100,000 cells) being injected. Care was taken to avoid blood vessels, and sufficient time was allowed between injections and for the retraction of the microsyringe. Following tumor cell inoculation, a 5 mm diameter coverslip was positioned over the injection site and secured with cyanoacrylate glue.

G. Characterization of BLEscope Current Consumption

We characterized the current consumption of the BLEscope during a continuous one-hour imaging experiment on an anesthetized mouse. During this experiment, the BLEscope was powered by a 3.7 V, 1700 mAh LiPo battery. The animal was securely positioned on the imaging platform, and the BLEscope focused on the cranial window. The IOS channel of the BLEscope was configured to operate in *streaming* mode at 1 fps under green LED illumination for 30 mins while measuring the voltage across R_1. This procedure was repeated with the FL channel of the BLEscope with the blue LED illuminated for the same duration (30 mins). Next, the IOS channel of the BLEscope was configured to operate in *single image capture* mode for 30 mins and the voltage across R_1 was measured. The same process was repeated with the FL channel activated for 30 mins while the BLEscope operated in *single capture* mode. To measure the voltage across R_1, we employed a digital oscilloscope in differential mode (Analog Discovery 3, Digilent Inc). We sampled the analog voltage at 500 Hz and recorded it in 64-bit floating point format. We computed the BLEscope's current consumption by dividing the voltage across R_1 by its resistance. The mean and standard deviation of the current consumed over 30 mins were then computed.

H. Fluorescence (FL) Imaging with the BLEscope

To assess the FL imaging capability of the BLEscope in the *streaming* mode under blue LED illumination, we imaged the transit of the intravenously administered fluorescent tracer, FITC-dextran, for 200 s at 1 fps. The FITC-dextran solution was prepared by dissolving 20 mg of FITC-dextran (MW=250 kDa, Sigma-Aldrich, Inc., MO) in 1 mL of saline, followed by thorough mixing and filtration. For this experiment, a mouse was anesthetized using an intraperitoneal injection of a 0.15 ml mixture of 80 mg/kg of ketamine and 8 mg/kg of xylazine and then secured on the imaging platform. With the BLEscope appropriately focused, image acquisition in the FL channel was started ~30 s before administration of ~400 µL of FITC-dextran via the tail vein and continued for ~170 s post-injection. Images were wirelessly transmitted to the laptop via BLE 5.2 at 1 fps. Given that the fluorescent tracer required one second to reach the arteries following injection, and 1.5 s to reach the veins [20], an image acquisition rate of 1 fps was sufficient to capture tracer transit within the cerebrovasculature. The FL channel of the BLEscope was also utilized to acquire images of GFP-expressing cells in two tumor-bearing mice. For these experiments, animals were anesthetized using 1.5% isoflurane in 1.5 L/min air, secured on the imaging platform and the BLEscope focused on the cranial window. The BLEscope was configured to operate in *streaming* mode to acquire 100 images over ~100 seconds at 1 fps from each tumor-bearing mouse with the entire tumor within the FOV.

I. Intrinsic Optical Signal (IOS) Imaging with the BLEscope

To assess the IOS imaging capability of the BLEscope, we conducted a carbogen inhalation experiment on the two brain tumor-bearing mice, as previously described in [21]. Since carbogen induced vasodilation occurs within 1-60 s [1], hemodynamic changes could be effectively imaged at 1 fps by employing the green LED illumination of the BLEscope. One mouse was imaged at ten days post-inoculation and another at thirteen days post-inoculation to ensure that the GFP signal from the brain tumor was detectable. For the carbogen challenge, the mouse was first anesthetized with 1.5%

isoflurane in 1.5 L/min air, via a Vapomatic Model 2 vaporizer (AM Bickford, Inc., NY). The mouse was then placed on the imaging platform, and its head was secured with the customized holder while continuously administering anesthesia as shown in **Figs. 5b** and **5c**. Via the FL channel, we then identified a FOV containing the GFP expressing brain tumor cells. Images from that FOV were then captured via the IOS channel using the *streaming mode* at 1 fps to establish a five-minute (300 s) baseline measurement during which the mouse breathed room air administered at 1.5 L/min. Next, IOS images were acquired for five minutes (300 s) during administration of carbogen, followed by a 15-minute (900 s) acquisition during which the mouse again breathed room air.

J. Image Processing

For visualizing the transit of the intravenously injected FITC-Dextran dye, each fluorescence (FL) image acquired over BLE was named according to its timestamp. Next, we co-registered the FL image stack using the "translational transformation" in the *MultiStackReg* plugin of ImageJ software [18, 19]. Then, to ensure a temporal resolution of 1 s, we employed the *interp3* function within MATLAB® and conducted three-dimensional (i.e. 2D+time) linear interpolation using the nearest neighbor algorithm, on the FL imaging data. This resulted in an FL image stack with a temporal resolution of 1 s. Next, a binary mask was generated by manually segmenting the blood vessels within the FOV with a stylus and tablet. This mask was multiplied with the FL image stack, so that only the transit of the FITC-dextran through the blood vessels was visualized. By estimating the transit parameters of intravenously administered fluorescent tracer FITC-Dextran within the vasculature, we could distinguish arterial and venous segments of the microvascular network within the FOV. This estimation involved applying the singular compartment recirculation (SCR) model [22] to the time-series of each pixel in the FL image stack. The SCR model was derived from the gamma variate model, which has been widely used in dynamic susceptibility-weighted contrast-enhanced (DSC) MRI [23] for the estimation of hemodynamic variables including relative cerebral blood volume (rCBV), relative cerebral blood flow (rCBF) and the mean transit time. The full SCR model can be expressed as:

$$SCR_F(t) = C + g(t) + \kappa \int_0^{\tau} g(\tau)\, d\tau + \varepsilon(t) \qquad (2)$$

Where $g(t) = A(t - t_0)^{\alpha} e^{-\frac{t-t_0}{\beta}}$ is the gamma-variate function, which is valid when $t > t_0$. A is an amplitude factor, t_0 is the onset time of the tracer, α is the rise exponent, β is the decay constant, C is an offset constant and κ is a multiplicative constant. $\varepsilon(t)$ is a noise estimate. By using the *3dNLfim* plugin in the Analysis of Functional Neuroimages (AFNI) software[24], the custom SCR model was fit to the FL image time-series spanning 170 s, and the arrival time and time-to-peak were computed for each pixel. Time-to-peak is the duration it takes for the concentration of the injected FITC dextran to reach a maximum concentration in the bloodstream, whereas the arrival time describes the time it took for the injected FITC-Dextran to first appear at each pixel location. To optimize the SCR model fit, a combination of Nelder-Mead [24] and Powell's NEWUOA [24] were used to minimize the sum square of error (SSE) between the SCR model and the FL data. A map of the coefficient of determination (R^2) was also generated to assess how well the SCR model fit the FL data, and was computed according to:

$$R^2 = 1 - \frac{SSE\big(SCR_F(t)\big)}{SSE\big(SCR_R(t)\big)} \qquad (3)$$

Where $SCR_R(t)$ is a reduced model consisting of only noise and offset terms. Using transit parameters like arrival time, time-to-peak from the pixel-wise fitted SCR(t), we identified an artery and a vein region-of-interest (ROI) within the FOV and plotted the changes in FL intensity for each, along with the mean SCR(t) of all the pixels those ROI.

The FL and IOS images acquired from the two brain-tumor bearing mice were also named using the timestamp of when it was received by the laptop. For each animal, these images were co-registered to the first image acquired at t=0, using "translational transformation" in the *StackReg* plugin of ImageJ [18, 19]. Next, a mean IOS image was computed from the pixel-wise average of the IOS images over the duration of the experiment. Next, all the FL images were co-registered with the mean IOS image using "translational transformation" in the ImageJ plugin *TurboReg* [18, 19]. We again employed the *interp3* function within MATLAB® to convert the FL and IOS images into image stacks with a temporal resolution of 1 s. After co-registration, an average FL image was also generated. We normalized the intensity histogram of the mean FL and IOS images using a 3% threshold to enhance the contrast of the tumor ROI relative to the background (i.e., non-tumor region). Subsequently, we analyzed specific ROI to assess the impact of brain tumor growth on the hemodynamic response to carbogen inhalation. The IOS time-series data from these ROI underwent median filtering with a sliding 1 min window. We chose 1/5th of the duration of carbogen administration, i.e. 1 minute, as the length of the sliding window to reduce noise. Next, we computed the change in the IOS signal (ΔIOS) with respect to an initial baseline (1-300 s) during the carbogen inhalation experiment. The baseline (i.e. mean during 1-300 s) IOS map was calculated as follows using IOS(t):

$$\mathrm{IOS}_{BL} = \frac{1}{300} \sum_{t=1\,s}^{t=300\,s} \mathrm{IOS(t)} \qquad (4)$$

The relative change of the IOS signal with respect to baseline at each time point "t", i.e. ΔIOS (t) was calculated as follows:

$$\Delta\mathrm{IOS(t)\%} = \frac{[\mathrm{IOS(t)} - \mathrm{IOS}_{BL}]}{\mathrm{IOS}_{BL}} \times 100 \qquad (5)$$

This enabled us to compare carbogen-induced changes in ΔIOS(t) between tumor and background (i.e. non-tumor regions) ROI for each of the brain tumor-bearing mice. We visualized the distribution of all ΔIOS% pixels during the carbogen inhalation challenge (i.e. 301-600 s) with box plots

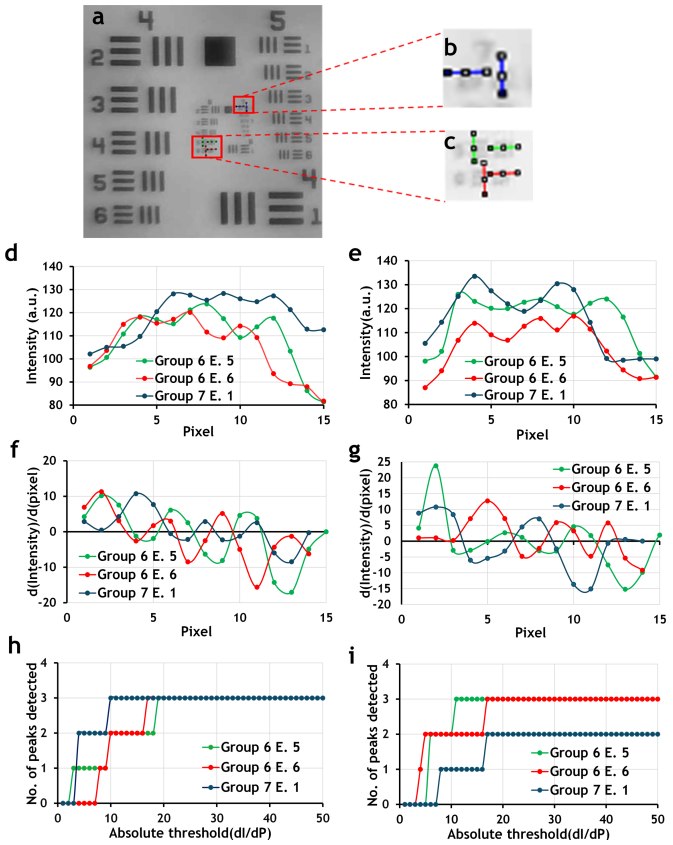

Fig. 6. BLEscope resolution characterization. (a) Image of a Positive 1951 USAF Optical Target acquired with the IOS channel of the BLEscope. The image was inverted to facilitate analysis of horizontal and vertical cross-sections across the line pairs of group 6 elements 5 and 6, and group 7 element 1. All of these are shown within the red rectangle. (b) and (c) show the magnified images of the FOV within the red rectangles, where (b) displays group 7 element 1, and (c) displays group 6 elements 5 and 6. The horizontal and vertical cross-sections across the line pairs of group 6 elements 5 and 6 are shown in green and red, respectively whereas they are shown in blue for group 7 element 1. (d) Cross-sectional profile along the horizontal lines. (e) Cross-sectional profile along the vertical lines. (f) Spatial derivative of the horizontal intensity profiles. (g) Spatial derivative of the vertical intensity profiles. (h) and (i) are plots of the no. of peaks that could be resolved at different thresholds. The threshold was varied from 0 to 50. Only 2 peaks could be resolved for group 7 element 1. Therefore, the finest resolution that could be resolved for BLEscope was 8.72 µm, and the measured width of a single line in group 4 element 1 was 31.25 µm. Additionally, the line width in group 4 element 1 in (a) was 24.22 µm. These measurements translate to a magnification of 0.75 for the BLEscope.

and used a two-tailed paired Wilcoxon Rank-Sum test (NCSS statistical software, $\alpha = 0.05$) to compare the IOS response to the carbogen challenge between tumor vs non-tumor ROI.

III. Results

A. Characterization of the optical performance of the BLEscope

Fig. 6a shows an image captured by the BLEscope that was utilized to assess spatial resolution. **Figs. 6b** and **6c**, present detailed views of specific line pair elements, namely group 7 element 1, and group 6 elements 5 and 6. Cross-sectional profiles across vertical and horizontal line pairs are illustrated in **Figs. 6d** and **6e**, respectively. **Fig. 6f** and **6g** depict the result

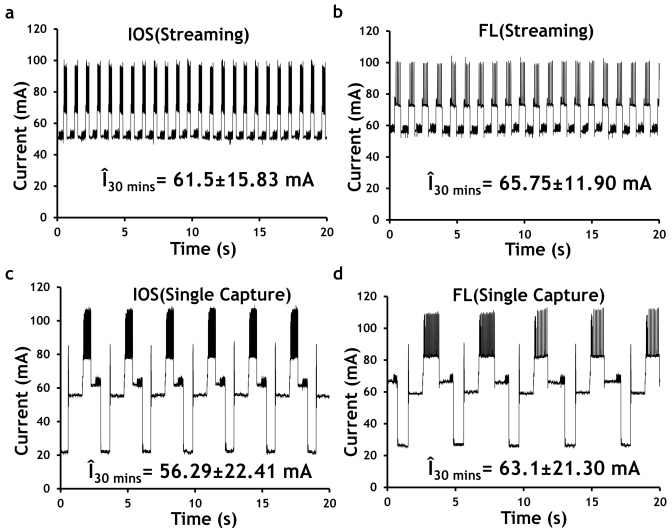

Fig. 7. Characterization of BLEscope current consumption while operating in different modes (*streaming* vs. *single capture*) for 2 channels (FL and IOS). Representative 20s excerpts from a 30-minute experiment indicating the current drawn by the BLEscope in *streaming mode* when acquiring images in (a) the IOS channel under green light illumination, and (b) the FL channel under blue light illumination. The confidence interval for current drawn by the BLEscope in (a) and (b) was 61.5±15.83 mA and 65.75 ± 11.9 mA, respectively. Representative 20-second excerpts from a 30-minute experiment indicating the current drawn by the BLEscope in *single capture* mode when acquiring images in the (c) IOS channel under green light illumination, and (d) FL channel under blue light illumination, respectively. The confidence interval for current drawn by the BLEscope in (c) and (d) was 56.29 ± 22.41 mA and 63.10 ± 21.30 mA, respectively.

of spatial differentiation of these cross-sectional profiles, highlighting local minima within each element. Further analysis in **Figs. 6h** and **6i** demonstrated the relationship between the number of detected peaks and absolute threshold, derived from the absolute values of the spatial derivative. It was evident that increasing thresholds resulted in the detection of more peaks, until the maximum number of peaks for each element was resolved. Notably, **Fig. 6i** shows that only two peaks of group 7 element 1 could be resolved, indicating an eventual plateau with increasing threshold. Consequently, the BLEscope successfully resolved 114 line pairs per millimeter (lp/mm) in group 6, element 6, corresponding to a spatial resolution of 8.72 µm. The magnification of the optical system was 0.75, with a field of view (FOV) of 1.9 mm².

B. Characterization of current consumption

The operation of the BLEscope's IOS channel in *streaming* mode at 1 fps was characterized by a current draw of 61.5±15.83 mA over 30 minutes. The excitation module consumed ~0.3 mA in this mode. **Fig. 7a** shows a 20-second excerpt from the 30 min experiment. Notably, the BLEscope exhibited a maximum current draw of 100.38 mA and a minimum of 47.40 mA in this mode. Similarly, for the FL channel, sustained operation in *streaming* mode yielded a current draw of 65.75±11.90 mA over the same 30-minute period. The excitation module consumed ~0.935 mA in this mode. **Fig. 7b** shows a 20-second segment from the 30 min experiment, highlighting a maximum and minimum current draw of 101.16 mA and 52.15 mA, respectively. Transitioning to *single image capture* mode when utilizing the IOS channel,

This article has been accepted for publication in IEEE Transactions on Biomedical Engineering. This is the author's version which has not been fully edited and content may change prior to final publication. Citation information: DOI 10.1109/TBME.2024.3467221

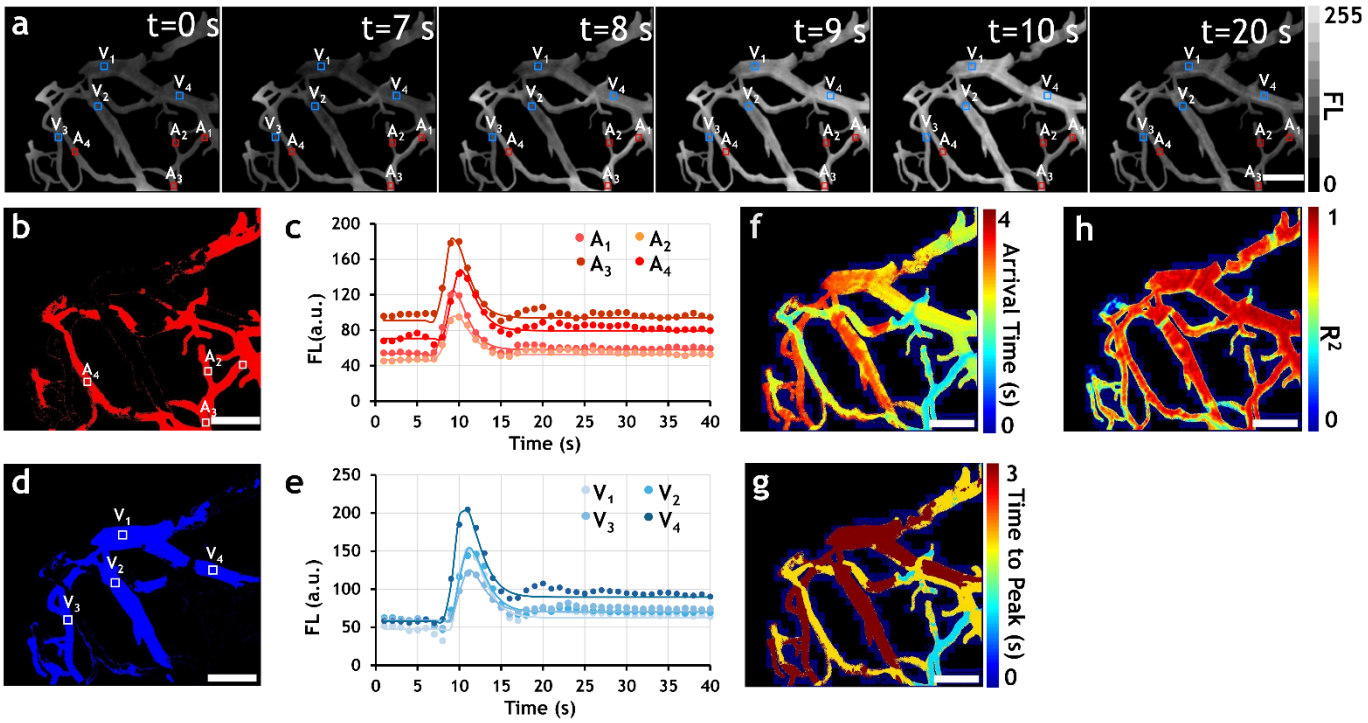

Fig. 8. BLEscope captures the vascular transit of FITC-dextran. (a) Fluorescence (FL) images acquired at 1fps during the transit of FITC-dextran through blood vessels over 200 s. FITC-dextran arrived in the arteries at t=7 s, and the veins at t=9 s, based on which arterial (red) and venous (blue) ROI were identified. (b) and (d) show maps of the arteries and veins differentiated on the basis of their times-to-peak. Arteries are shown in red, and veins in blue, with respective ROI from (a) overlaid in white. Representative 40 s FL intensity vs. time plots for arterial (c) and venous (e) ROI, from the 200 s acquisition. A gamma-variate function (solid lines in (c) and (e)) was fit to the FL time-series data (dots) for arterial and venous ROI, from which arrival time and time-to-peak were computed. Pseudo-color maps of: (f) arrival time of the FITC-dextran, and (g) time-to-peak in the blood vessels. (h) Map of the positive correlation coefficients (R^2) indicating the fit quality of the gamma-variate function. The scale bar in all images = 0.22 mm.

the BLEscope displayed a current draw of 56.29±22.41 mA. The excitation module consumed ~0.3 mA in this mode. **Fig. 7c** presents a 20-second snapshot from the 30-minute experiment. Meanwhile, when operating in *single capture mode* with the FL channel, the BLEscope drew a current of 63.2±21.30 mA over 30 minutes. The excitation module consumed ~0.935 mA in this mode. **Fig. 7d** provides a 20-second excerpt from the same 30-minute experiment. Across all configurations (FL/IOS) and acquisition modes (streaming/single image capture), the BLEscope consistently exhibited a maximum current draw of ~66 mA. This efficiency implied that continuous imaging could be sustained for ~1.5 hours on a 100 mAh battery.

C. *BLEscope captures the vascular transit of FITC-dextran*

We utilized the FL channel of the BLEscope for real-time imaging of the transit of intravenously administered FITC-dextran. **Fig. 8a** illustrates sequential FL images acquired with the BLEscope (see **Suppl. Movie 1**) along with four arterial (red) and four venous (blue) ROI. **Figs. 8b** and **8d** show the arterial and venous segments, respectively, that were identified based on their times-to-peak. **Figs. 8c** and **8e** show a 40 s excerpt from the 200 s tracer time-series, wherein one can visualize the tracer concentration peaking within each arterial and venous ROI. By fitting the tracer kinetics to the SCR model, we successfully discriminated between the arterial and venous transits of FITC-dextran. We observed a lag of ~1 s between the peaking of the FL signal within the veins relative to the arteries. **Fig. 8f** is a pseudo-color map of the range of arrival times of FITC-dextran within the blood vessels, whereas **Fig. 8g** is a pseudo-color map illustrating the times required for the FL signal to peak within the blood vessels. Finally, **Fig. 8h** illustrates the positive correlation coefficients for the pixel-wise fitting of the SCR model to each fluorescent intensity vs. time curve, confirming that this model fits the data well.

D. *Multicontrast imaging capability of BLEscope reveals differential hemodynamics in the brain tumor microenvironment*

The BLEscope's FL channel enabled us to image GFP-expressing brain tumor cells in vivo, as shown in **Figs. 9a** and **9d.** The same FOV was also imaged with the IOS channel, and **Figs. 9b** and **9e** show the mean IOS maps acquired over 25 mins, for each animal (see **Suppl. Movies 2** and **3**). To assess carbogen-induced hemodynamic changes, four ROI were selected (**Figs. 9b** and **9e**) and their respective IOS time-series plotted in **Figs. 9c** and **9f**. These ROI were: tumor; background (i.e. non-tumor pixels); a tumor-associated blood vessel; and a background (i.e. non-tumor region) blood vessel distant from the tumor. **Figs. 9c** and **9f** reveals that the hemodynamic response of the tumor region and the tumor-associated blood vessels to carbogen inhalation was attenuated compared to that of the background and background (i.e., non-tumor region) blood vessel, respectively. To quantify this attenuation, **Figs. 9g** and **9i** show corresponding time series for the tumor and background ROI (i.e. ΔIOS%) that were normalized to respect

This article has been accepted for publication in IEEE Transactions on Biomedical Engineering. This is the author's version which has not been fully edited and content may change prior to final publication. Citation information: DOI 10.1109/TBME.2024.3467221

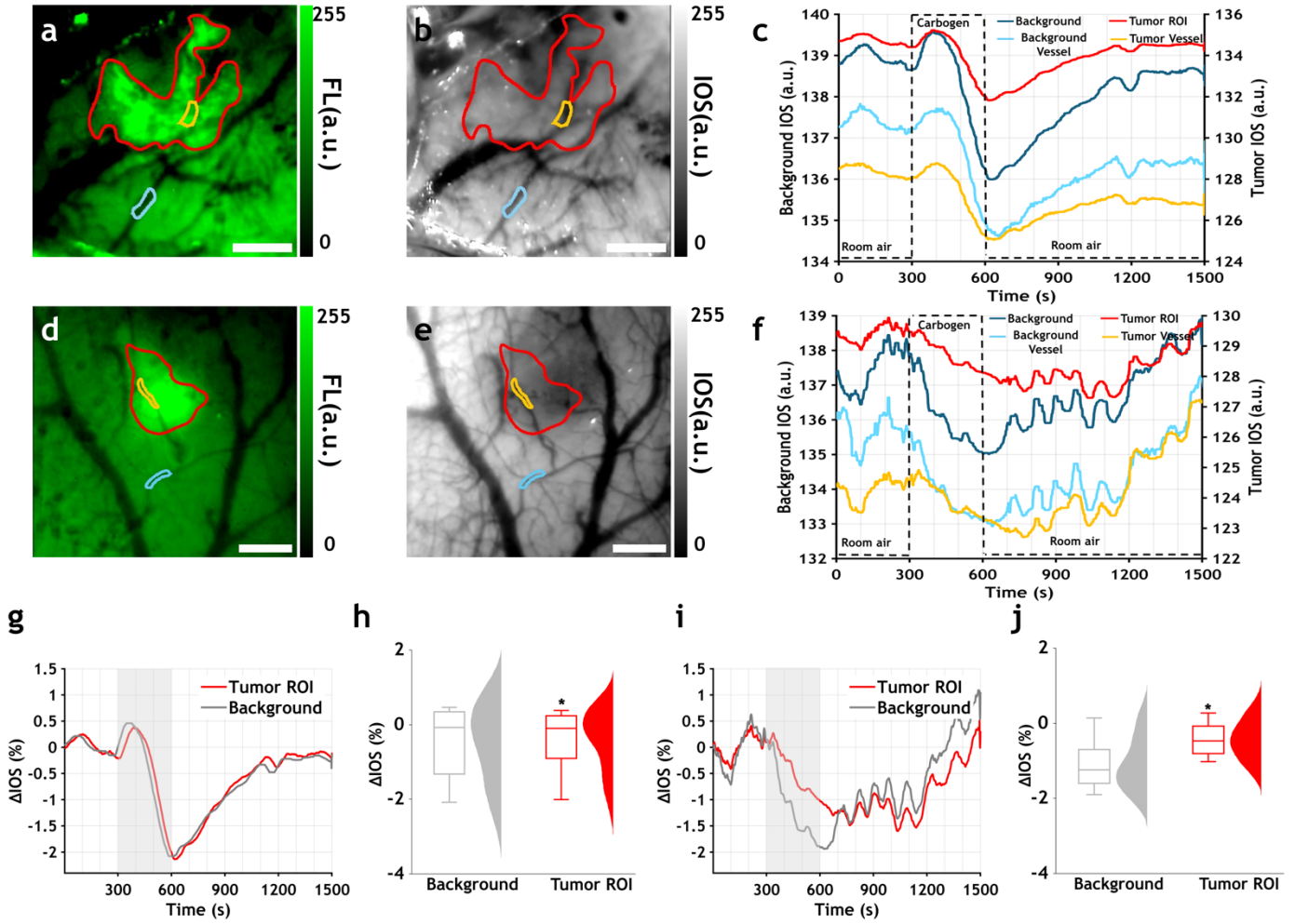

Fig. 9. Multicontrast imaging capability of BLEscope reveals differential hemodynamics in the brain tumor microenvironment. (a) and (d) are the mean FL images of GFP-expressing brain tumor cells from the third (i.e. post-inoculation day 10) and fourth mouse (i.e. post-inoculation day 13), respectively. The animals were made to breathe room air for 300 s, carbogen gas (i.e. 95% O_2 and 5% CO_2) for the next 300 s, and room air again for 900 s. ROI were chosen to map hemodynamic changes with the IOS channel. (b) and (e) are mean IOS images for the same FOV as in (a) and (d), respectively. (c) and (f) are IOS time-series representing hemodynamic changes in background (i.e. non-tumor region), background blood vessel, tumor (secondary y-axis) and tumor blood vessel (secondary y-axis) ROI. The carbogen administration interval is indicated by hatched lines. Panels (g) and (i) show ΔIOS(t)% for the tumor, and background ROI in response to carbogen inhalation for each animal. Box plot and histogram for background and tumor ROI are shown in (h) and (j) for post-inoculation day 10 and 13, respectively. There was a significant difference ($p<<0.01$) between background and tumor ΔIOS% for both post-inoculation time points. Scale bar = 0.22 mm.

to the mean of their pre-carbogen baselines (also see **Suppl. Movies 4** and **5**). **Figs. 9h** and **9j** show box and histogram plots of the distributions of ΔIOS% during carbogen inhalation. Although there was a significant difference ($p<<0.01$) between background and tumor ΔIOS% for both post-inoculation time points, the difference in the carbogen response between these two regions was amplified in the later-stage tumor bearing mouse. Specifically, the median and inter-quartile range (IQR) for non-tumor vs. tumor ΔIOS% was -0.07% (-1.32% to 0.34%) vs. -0.10% (-0.90% to 0.24%) in the early-stage brain tumor bearing mouse, and -1.24% (-1.59% to -1.71%) vs. -0.47% (-0.81% to -0.08%) in the late-stage brain tumor bearing mouse. Collectively, these findings indicate that tumor progression may have impacted the hemodynamic response of this brain region, and made it less responsive to vasodilatory stimuli, such as carbogen inhalation.

IV. Discussion

Here we report the implementation of the first-ever Bluetooth-capable wireless microscope prototype called BLEscope. The BLEscope's BLE5.2 architecture enabled wireless control of the microscope as well as remote image acquisition for all the imaging experiments in this study. Using MATLAB®, we successfully implemented *single image capture* and *streaming* wireless transfer modes. This enabled FL and IOS contrast-based imaging experiments of head-fixed mice that clearly demonstrated the feasibility of wireless in vivo functional imaging. Despite the BLEscope being limited to acquiring images at 1 fps, we successfully tracked the transit of a fluorescent tracer through the cerebrovasculature and imaged fluorescently labeled GL261 tumor cells in a preclinical model of brain cancer. Additionally, via the IOS channel, we were able to measure vasodilation resulting from carbogen inhalation and successfully differentiated the responses of brain tumor-associated and surrounding blood vessels. In the future, such data could shed light on how brain tumor progression affects

microvascular hemodynamics. Moreover, the results from our study were consistent with other reports demonstrating the well-known structural and functional differences between tumor-associated and background (i.e., non-tumor region) (or healthy) blood vessels [25].

We determined that the BLEscope drew an average ~66 mA in *streaming* mode, implying that one could conduct ~1.5 hours of continuous imaging at 1 fps with a 100 mAh battery. This exceeds the 15 min of imaging currently achievable with the miniScope [4] using a similar battery, wherein images are saved to an onboard MicroSD card. It is worth noting that SD cards draw ~20-100 mA at 3.3 V during data transfer [26]. In contrast, the RSL10 module exhibited lower power consumption, with a current draw of ~4.6 mA during data transmission, and ~3 mA while receiving data at 3 V, as described in [11]. Moreover, BLE 5.2 exhibited several distinct advantages for long-term functional imaging over other wireless technologies such as the older NTSC protocol employed by the Finchscope [3], and wireless video streaming with LoRa backscatter [7, 8, 27]. For example, NTSC is largely obsolete in the digital era, rendering it unsuitable for high-quality multimedia transmission [6]. Also, it is important to note that of ~66 mA of current consumption in *streaming* mode with the FL channel activated, the LED consumed ~0.9 mA, while the RSL10 drew ~7.6 mA at 3 V [11], and the image sensor consumed 2.4 mA at 1fps [12]. Collectively, these data indicate that the LEDs were not the BLEsope components that consumed the most current.

LoRaWAN (Long Range Wide Area Networks) [28], although promising, has limited transceiving rates (e.g. 18-37 kbps) [8], making it inadequate for high-bandwidth video and image transmission. In contrast, BLE 5.2 offers data rates of up to 2 Mbps that are well-suited for real-time or near-real-time video and image transmission [11]. Moreover, BLE's data packet optimization minimized energy consumption, which was a critical factor for battery-operated devices like the BLEscope. Finally, BLE 5.2's well-established market presence ensures readily available hardware and robust developer support, further solidifying its utility for wireless functional imaging applications, as well as its integration into IoT-like setups.

Relative to other low-power wireless technologies like Zigbee, BLE 5.2 offers power-efficient data rates of up to 2 Mbps that surpass Zigbee's typical transmission data rate of 250 Kbps [29]. Moreover, as demonstrated here, BLE 5.2 enabled the seamless integration of the BLEscope with other wireless devices such as smartphones (and laptops), which simplified user connectivity and remote microscope operability compared to Zigbee.

The choice of image sensor also played an important role in BLEscope's architecture. Most of the image sensors employed in the current generation of miniscopes exhibit lower quantum efficiency than the ARX3A0 image sensor, while consuming more power. For example, the PYTHON480 sensor used by the UCLA miniscope [2] had a quantum efficiency of just above 50% in the 500-700 nm range, while consuming 260 mW at 60 fps. Similarly, the miniScope [4] employed the MT9V022 sensor, which had a quantum efficiency close to 50% in the 550-650 nm range, consuming approximately 320 mW of power at 60 fps. In contrast, the ARX3A0 sensor consumed only 67 mW at 120 fps, 12.5 mW at 30 fps, and just 3.2 mW at 1 fps [12], while providing a quantum efficiency of 90% in 450-550 nm range.

The ARX3A0 image sensor's high quantum efficiency proved very useful for the brain tumor imaging experiment. In this experiment, erythrocyte-bound hemoglobin that provides IOS contrast, was abundant in the highly vascularized brain tumor microenvironment and cortex. This abundance enabled the acquisition of IOS images of microvascular structure with high signal-to-noise ratio (SNR). Conversely, the low number of fluorescent brain tumor cells within the same region resulted in FL images which only permitted visualizing the tumor margins against its background with a lower SNR. However, as can be seen in **Figs. 9a** and **d**, the SNR of the tumor cells was satisfactorily high due to the 90% quantum efficiency (QE) of the ARX3A0 CMOS image sensor in 450-550 nm range, making it ideal for FL and IOS imaging applications. The higher QE of the image sensor significantly enhanced the SNR with which FL imaging could be conducted by increasing the photon detection efficiency. Additionally, the high QE reduced the exposure time, minimizing motion-induced blur and photobleaching of the fluorescent brain tumor cells, thereby preserving image quality. The enhanced photon detection capabilities were particularly crucial for low-light conditions typical of FL imaging, capturing finer details and allowing for better spatial resolution. These factors made the ARX3A0 a suitable image sensor for FL and IOS imaging applications. Additionally, the ARX3A0 sensor interfaced with the SPCV1100A ISP via the recently developed MIPI CSI-2, consuming less power (3 mW) than Himax's HM01B0 CMOS image sensor, which also communicates over MIPI CSI-2 but consumed 4 mW at 1 fps [30].

While our in vivo experiments demonstrated the utility of the BLEscope, we anticipate several enhancements to result from miniaturizing this wireless architecture. For example, a major limitation of employing an off-the-shelf (RSL10) architecture for the BLEscope was that control of the exposure time and gain of the ARX3A0 IAS modules were limited because they were automatically set by SPCV1100A ISP. To change these settings the user would need to write to the flash program memory of the SPCV1100A ISP each time. Moreover, the efficiency and current control precision of our excitation module which comprised of a current mirror circuit was not comparable to that achievable with commercially available LED driver ICs. Additionally, under 530±20 nm illumination, our tissue imaging depth was limited to an estimate of ~500 µm [13]. Therefore, in our miniaturized prototype of this architecture, we would first enable direct control of these features of the IAS module over BLE5.2 with the help of a GUI. Second, we intend to redesign the current optical front end to enable remote focusing. We will employ an electronic lens so that focusing can be controlled remotely by the RSL10 [11] via instructions

sent over BLE 5.2. Third, although we have not used the accelerometer embedded in this architecture, we intend to use it in the miniaturized prototype to monitor the animal's motion while simultaneously imaging its brain. Fourth, in our miniaturized architecture, we plan to include the low-power FAN54120 (FAN54120uc420x) component to enable the recharging of the LiPo battery via a USB interface. This will eliminate the need for frequent LiPo battery replacements by allowing us to recharge the battery while it is still attached to the animal. Fifth, we will add an additional channel to our BLEscope by equipping it with a near-infrared (NIR) LED to enhance its maximum imaging depth in tissue [31]. Finally, we will replace the current mirror circuit with an onboard LED driver, which will also be used to wirelessly control LEDs and their switching. Once miniaturized, this architecture will be able to support long-term functional imaging of the murine brain to a depth of more than ~500 μm and provide new insights into brain diseases.

V. Conclusion

In this paper, we reported the implementation of a multicontrast microscope (i.e. BLEscope) driven by the low-power BLE 5.2 communication protocol for wireless in vivo functional imaging. We demonstrated the potential of the BLEscope via MATLAB®-implemented image acquisition modes and in vivo functional imaging experiments on mice. The BLEscope's low current consumption (~66 mA) and use of BLE 5.2 highlighted its superiority to other wireless technologies in terms of data rates and power efficiency. The use of BLE 5.2 also ensured compatibility with other wireless devices for remote microscope operation. Finally, the integrated ARX3A0 image sensor further enhanced BLEscope's performance by providing high quantum efficiency (90 %) combined with low power (3.2 mW) operation. Future miniaturization of the current architecture of the BLEscope would enhance its operation and functionality in terms of exposure and focus adjustments, motion monitoring, battery recharging, and illumination control. We believe that a miniaturized BLEscope architecture holds great promise for wireless functional imaging and would provide invaluable insights into brain function. Furthermore, following appropriate modifications and FDA approval, the BLEscope could be utilized in the clinic as a wire-free image acquisition device to conduct intraoperative imaging [32, 33], or as an implantable device in a 3D-printed skull cap or bone graft [34, 35] to enable real-time imaging of cerebral hemodynamics.

References

[1] J. Senarathna, H. Yu, C. Deng, A. L. Zou, J. B. Issa, D. H. Hadjiabadi, S. Gil, Q. Wang, B. M. Tyler, N. V. Thakor, and A. P. Pathak, "A miniature multi-contrast microscope for functional imaging in freely behaving animals," *Nat Commun,* vol. 10, no. 1, pp. 99, Jan 9, 2019.

[2] D. Aharoni, B. S. Khakh, A. J. Silva, and P. Golshani, "All the light that we can see: a new era in miniaturized microscopy," *Nat Methods,* vol. 16, no. 1, pp. 11-13, Jan, 2019.

[3] W. A. Liberti, L. N. Perkins, D. P. Leman, and T. J. Gardner, "An open source, wireless capable miniature microscope system," *J Neural Eng,* vol. 14, no. 4, pp. 045001, Aug, 2017.

[4] G. Barbera, B. Liang, L. Zhang, Y. Li, and D. T. Lin, "A wireless miniScope for deep brain imaging in freely moving mice," *J Neurosci Methods,* vol. 323, pp. 56-60, Jul 15, 2019.

[5] A. de Groot, B. J. G. van den Boom, R. M. van Genderen, J. Coppens, J. van Veldhuijzen, J. Bos, H. Hoedemaker, M. Negrello, I. Willuhn, C. I. De Zeeuw, and T. M. Hoogland, "NINscope, a versatile miniscope for multi-region circuit investigations," *Elife,* vol. 9, Jan 14, 2020.

[6] T. Kanada, K. Hakoda, and E. Yoneda, "Snr Fluctuation and Non-Linear Distortion in Pfm Optical Ntsc Video Transmission-Systems," *Ieee Transactions on Communications,* vol. 30, no. 8, pp. 1868-1875, 1982.

[7] "The LoRa Alliance Home Page," 08/08/24; https://lora-alliance.org/.

[8] M. Ayoub Kamal, M. M. Alam, A. A. B. Sajak, and M. Mohd Su'ud, "Requirements, Deployments, and Challenges of LoRa Technology: A Survey," *Comput Intell Neurosci,* vol. 2023, pp. 5183062, 2023.

[9] S. Naderiparizi, M. Hessar, V. Talla, S. Gollakota, and J. R. Smith, "Towards Battery-Free HD Video Streaming," *Proceedings of the 15th Usenix Symposium on Networked Systems Design and Implementation (Nsdi'18)*, pp. 233-247, 2018.

[10] Onsemi, "Evaluation Board | SECO-RSL10-CAM-GEVB," 2021.

[11] Onsemi, "RSL10 Datasheet," Oct. 1, 2022.

[12] Onsemi, "1/10.3-inch 0.3 Mp Digital Image Sensor," Feb 2022.

[13] Y. Ma, M. A. Shaik, S. H. Kim, M. G. Kozberg, D. N. Thibodeaux, H. T. Zhao, H. Yu, and E. M. Hillman, "Wide-field optical mapping of neural activity and brain haemodynamics: considerations and novel approaches," *Philos Trans R Soc Lond B Biol Sci,* vol. 371, no. 1705, Oct 5, 2016.

[14] E. M. Hillman, "Optical brain imaging in vivo: techniques and applications from animal to man," *J Biomed Opt,* vol. 12, no. 5, pp. 051402, Sep-Oct, 2007.

[15] J. H. Park, J. Platisa, J. V. Verhagen, S. H. Gautam, A. Osman, D. Kim, V. A. Pieribone, and E. Culurciello, "Head-mountable high speed camera for optical neural recording," *J Neurosci Methods,* vol. 201, no. 2, pp. 290-5, Oct 15, 2011.

[16] Onsemi, "Regulator - TinyPower , Buck-Boost: 2.5 A, 1.8 MHz," 2019.

[17] Onsemi, "7-Channel PMIC with 2 DC-DC Converters, 5 LDOs and a Triple Input 10 Bits ADC," 2020.

[18] J. Schindelin, I. Arganda-Carreras, E. Frise, V. Kaynig, M. Longair, T. Pietzsch, S. Preibisch, C. Rueden, S. Saalfeld, B. Schmid, J. Y. Tinevez, D. J. White, V. Hartenstein, K. Eliceiri, P. Tomancak, and A. Cardona, "Fiji: an open-source platform for biological-image analysis," *Nat Methods,* vol. 9, no. 7, pp. 676-82, Jun 28, 2012.

[19] C. A. Schneider, W. S. Rasband, and K. W. Eliceiri, "NIH Image to ImageJ: 25 years of image analysis," *Nat Methods,* vol. 9, no. 7, pp. 671-5, Jul, 2012.

[20] V. Kalchenko, D. Israeli, Y. Kuznetsov, and A. Harmelin, "Transcranial optical vascular imaging (TOVI) of cortical hemodynamics in mouse brain," *Sci Rep,* vol. 4, pp. 5839, Jul 25, 2014.

[21] L. Bentzen, S. Keiding, M. R. Horsman, T. Gronroos, S. B. Hansen, and J. Overgaard, "Assessment of hypoxia in experimental mice tumours by [18F]fluoromisonidazole PET and pO2 electrode measurements. Influence of tumour volume and carbogen breathing," *Acta Oncol,* vol. 41, no. 3, pp. 304-12, 2002.

[22] V. Patil, and G. Johnson, "An improved model for describing the contrast bolus in perfusion MRI," *Med Phys,* vol. 38, no. 12, pp. 6380-3, Dec, 2011.

[23] G. H. Jahng, K. L. Li, L. Ostergaard, and F. Calamante, "Perfusion magnetic resonance imaging: a comprehensive update on principles and techniques," *Korean J Radiol,* vol. 15, no. 5, pp. 554-77, Sep-Oct, 2014.

[24] R. W. Cox, "AFNI: software for analysis and visualization of functional magnetic resonance neuroimages," *Comput Biomed Res,* vol. 29, no. 3, pp. 162-73, Jun, 1996.

[25] R. W. Pak, D. H. Hadjiabadi, J. Senarathna, S. Agarwal, N. V. Thakor, J. J. Pillai, and A. P. Pathak, "Implications of neurovascular uncoupling in functional magnetic resonance imaging (fMRI) of brain tumors," *J Cereb Blood Flow Metab,* vol. 37, no. 11, pp. 3475-3487, Nov, 2017.

[26] "SD Card Wikipedia Page," https://en.wikipedia.org/wiki/SD_card.

[27] M. U. Sheikh, B. Xie, K. Ruttik, H. Yigitler, R. Jantti, and J. Hamalainen, "Ultra-Low-Power Wide Range Backscatter Communication Using Cellular Generated Carrier," *Sensors (Basel),* vol. 21, no. 8, Apr 10, 2021.

[28] H. Ruotsalainen, G. Shen, J. Zhang, and R. Fujdiak, "LoRaWAN Physical Layer-Based Attacks and Countermeasures, A Review," *Sensors (Basel),* vol. 22, no. 9, Apr 19, 2022.

[29] C. H. Tseng, "Coordinator Traffic Diffusion for Data-Intensive Zigbee Transmission in Real-time Electrocardiography Monitoring," *IEEE Trans Biomed Eng,* vol. 60, no. 12, pp. 3340-6, Dec, 2013.

[30] Himax, "HM01B0-MNA-Datasheet," 2019.

[31] T. Wang, Y. Chen, B. Wang, X. Gao, and M. Wu, "Recent Progress in Second Near-Infrared (NIR-II) Fluorescence Imaging in Cancer," *Biomolecules,* vol. 12, no. 8, Jul 28, 2022.

[32] C. Jiang, A. Bhattacharya, J. R. Linzey, R. S. Joshi, S. J. Cha, S. Srinivasan, D. Alber, A. Kondepudi, E. Urias, B. Pandian, W. N. Al-Holou, S. E. Sullivan, B. G. Thompson, J. A. Heth, C. W. Freudiger, S. S. S. Khalsa, D. R. Pacione, J. G. Golfinos, S. Camelo-Piragua, D. A. Orringer, H. Lee, and T. C. Hollon, "Rapid Automated Analysis of Skull Base Tumor Specimens Using Intraoperative Optical Imaging and Artificial Intelligence," *Neurosurgery,* vol. 90, no. 6, pp. 758-767, Jun 1, 2022.

[33] M. Oelschlagel, T. Meyer, U. Morgenstern, H. Wahl, J. Gerber, G. Reiss, E. Koch, G. Steiner, M. Kirsch, G. Schackert, and S. B. Sobottka, "Mapping of language and motor function during awake neurosurgery with intraoperative optical imaging," *Neurosurg Focus,* vol. 48, no. 2, pp. E3, Feb 1, 2020.

[34] J. Portnow, B. Badie, M. Suzette Blanchard, J. Kilpatrick, R. Tirughana, M. Metz, S. Mi, V. Tran, J. Ressler, M. D'Apuzzo, K. S. Aboody, and T. W. Synold, "Feasibility of intracerebrally administering multiple doses of genetically modified neural stem cells to locally produce chemotherapy in glioma patients," *Cancer Gene Ther,* vol. 28, no. 3-4, pp. 294-306, Apr, 2021.

[35] K. S. Mitchell, W. Anderson, T. Shay, J. Huang, M. Luciano, J. I. Suarez, P. Manson, H. Brem, and C. R. Gordon, "First-In-Human Experience With Integration of Wireless Intracranial Pressure Monitoring Device Within a Customized Cranial Implant," *Oper Neurosurg (Hagerstown),* vol. 19, no. 3, pp. 341-350, Sep 1, 2020.